Multilevel perspective on high-order harmonic generation in solids

Mengxi Wu, Dana A. Browne, Kenneth J. Schafer, and Mette B. Gaarde[*]

Department of Physics and Astronomy, Louisiana State University, Baton Rouge, Louisiana 70803-4001, USA

(Received 5 August 2016; published 5 December 2016)

We investigate high-order harmonic generation in a solid, modeled as a multilevel system dressed by a strong infrared laser field. We show that the cutoff energies and the relative strengths of the multiple plateaus that emerge in the harmonic spectrum can be understood both qualitatively and quantitatively by considering a combination of adiabatic and diabatic processes driven by the strong field. Such a model was recently used to interpret the multiple plateaus exhibited in harmonic spectra generated by solid argon and krypton [G. Ndabashimiye *et al.*, Nature **534**, 520 (2016)]. We also show that when the multilevel system originates from the Bloch state at the Γ point of the band structure, the laser-dressed states are equivalent to the Houston states [J. B. Krieger and G. J. Iafrate, Phys. Rev. B **33**, 5494 (1986)] and will therefore map out the band structure away from the Γ point as the laser field increases. This leads to a semiclassical three-step picture in momentum space that describes the high-order harmonic generation process in a solid.

I. INTRODUCTION

Beginning with its first observation in rare gases almost 30 years ago [1], high-order harmonic generation (HHG) has become the foundation for attosecond science through a series of advances at the fundamental as well as the applied level [2–9]. Since the turn of the millennium, attosecond pulses produced via gas-phase HHG have become a successful tool for the study of ultrafast dynamics in atoms, molecules, and biological systems [10–13]. The recent observation of HHG from bulk solids, displaying a plateau of harmonics that ends in a high-frequency cutoff [14–20], has generated considerable interest given its potential as both a compact, next-generation ultrafast light source in the extreme ultraviolet (XUV) and the promise of applying HHG spectroscopic techniques to correlated electron dynamics in bulk materials [17].

The mechanism for HHG in solids has been intensely debated [21–30], and a conceptual picture of the generation process, augmented by new experimental results [16,17,19,20,31], is only slowly beginning to emerge. In momentum space, the discussion has centered on the relative contributions of interband and intraband processes to the driven nonlinear current that gives rise to the harmonic radiation [14,16,23–26]. A consensus is forming that while intraband contributions are important for harmonics with energies below the band gap [16], interband processes generally dominate the higher harmonics that span the plateau region [26,27]. In real space, Vampa and collaborators [23] have proposed a three-step semiclassical model in which a localized electron and hole pair are accelerated away from and recollide with each other after traversing many lattice cells, in analogy with the gas-phase three-step model of HHG [4,5].

While most of the works discussed above have described the strong-field dynamics using only a valence band and the lowest-lying conduction band, recent experimental and theoretical findings indicate another layer of complexity in the HHG process: Ndabashimiye *et al.* [20] directly compared the harmonics from argon and krypton in their solid phase and their gas phase and found that the solid HHG spectra exhibited multiple plateaus with the highest cutoff energies far exceeding those found in the gas phase for the same laser intensity. The multiple plateaus and their relative strengths and cutoff energies were reproduced using a multilevel model that takes into account the coupling between the valence band and several conduction bands at the high symmetry (Γ) point in solid argon [20].

In this paper we explore in detail the multilevel model used in [20] to calculate the HHG spectrum from a solid interacting with a strong, mid-infrared laser field. We show that the appearance of multiple plateaus in the harmonic spectrum from such a system can be understood both qualitatively and quantitatively, and we derive predictions for the cutoff energies and the relative strengths of the different plateaus. We begin by showing that a multilevel system is a natural basis in which to consider harmonic generation in a solid, because when the time-dependent Schrödinger equation (TDSE) in a periodic system is solved in the velocity gauge the different values of the crystal momentum k_0 remain uncoupled even in the presence of a laser field [21,32]. The band structure of the solid can thus be represented as a collection of independent multilevel systems, and the dynamics in the solid is given by the sum of the dynamics of each k_0 value represented in the initial wave function. Here we concentrate on the dynamics that result from the simplest possible initial condition, in which a single Bloch state with $k_0 = 0$ (Γ point) is considered so that the initial electron wave function is maximally delocalized. In [26] we showed that this very simple condition reproduces the characteristics of inter- and intraband contributions to HHG and their relative importance to low- and high-order harmonics. We interpret the electron dynamics in the multilevel system in terms of the time-dependent eigenstates of the laser-dressed system, the adiabatic states, and we show how HHG proceeds through a combination of adiabatic and diabatic processes involving the dressed states, similarly to what has been discussed, for instance, in [24]. We use the evolution of the adiabatic states to derive predictions for the cutoff energies and relative strengths of each plateau supported by the multilevel system.

_____

[*]gaarde@phys.lsu.edu

After discussing HHG in multilevel systems, we show that when the multilevel system is constructed from the energy levels and their transition matrix elements for a periodic potential at $k_0 = 0$, the adiabatic states will recover the full $k_0 \neq 0$ band structure of that solid, if we allow the crystal momentum to increase with the vector potential of the field, similar to what is done in the Houston-state treatment in Ref. [32]. This correspondence between the adiabatic states and the band structure leads us to a semiclassical, three-step picture for harmonic generation in a solid, in momentum space. In this picture, the delocalized electron first tunnels from the valence band (VB) to the conduction band (CB) at the zero of the vector potential and then is accelerated on the CB as the vector potential increases and decreases through an optical half-cycle. The coherence between the VB and the CB populations leads to the emission of XUV radiation, with photon energies corresponding to the instantaneous energy difference between the VB and the CB. This means that every energy below the cutoff energy is emitted twice in each half-cycle. This picture also allows us to predict that for a one-dimensional (1D) multiband system, the maximum cutoff energy of each plateau will be limited by the maximum band gap between the VB and the highest-lying CB involved in producing that plateau. This extends the cutoff limitation proposed in [28] and [24] for two-band systems to a multiband system exhibiting multiple plateaus in the harmonic spectrum.

The paper is organized as follows: In Sec. II we introduce the theoretical framework that the remainder of the paper is based on, namely, the solution of the single-active-electron TDSE in a 1D solid interacting with a strong field, and we discuss our initial condition of a delocalized electron wave function. In Sec. III we use the simplest multilevel system—the two-level system—to review the formalism for how to think about HHG in a multilevel system both at the qualitative level, using a three-step picture, and at the quantitative level, in terms of predictions for the strength and extent (cutoff energy) of the plateau. In Sec. IV we study HHG in a multilevel system consisting of four or more levels, which, as discussed above, leads to the appearance of multiple plateaus in the harmonic spectrum. We extend the two-level formulas and derive expressions for the cutoff energies and relative strengths of the different plateaus. Finally, in Sec. V we show the connection between the adiabatic states of the dressed multilevel system and the band structure of the model solid and the resulting semiclassical picture of HHG in solids. Section VI presents a brief summary of our results. We use atomic units throughout this paper.

II. SOLVING THE TDSE FOR A 1D SOLID

Strong-field processes in solids are often modeled by solving the TDSE in the velocity gauge using the dipole approximation [21,24–26],

$$i \frac{\partial}{\partial t} |\psi(t)\rangle = \left(\frac{\hat{p}^2}{2} + V(\hat{x}) + \vec{A}(t) \cdot \hat{p} \right) |\psi(t)\rangle, \quad (1)$$

where $V(\hat{x})$ is a periodic, one-electron pseudopotential that can be calculated approximately, for instance, from density functional theory. $\vec{A}(t)$ is the vector potential of the laser pulse in the dipole approximation, where we assume that the laser

wavelength (often 1 μm or greater) is much larger than the lattice constant, meaning that we can take $\vec{A}$ to be coordinate independent. Throughout the paper, we consider a 1D model, so that the $\hat{x}$ and $\vec{A}$ reduce to 1D quantities. This models a thin crystal with one of the transverse crystal directions (for example, the $\Gamma - X$) aligned with the laser polarization.

When solving Eq. (1) in the independent particle model it is convenient to expand the time-dependent wave function in the eigenstates of the field-free Hamiltonian, i.e., the Bloch-state basis

$$|\psi_{k_0}(t)\rangle = \sum_n C_{nk_0}(t) |\phi_{nk_0}\rangle, \quad (2)$$

where $|\phi_{nk_0}\rangle$ is the Bloch state for a specific crystal momentum k_0 in the nth band. This expansion allows us to take advantage of the fact that within the dipole approximation each crystal momentum channel k_0 is independent [21], even in the presence of the field. After expanding in the Bloch-state basis, the TDSE in each crystal momentum channel is

$$i \frac{\partial}{\partial t} C_{nk_0} = C_{nk_0} \varepsilon_n(k_0) + A(t) \sum_{n'} C_{n'k_0} p_{k_0}^{nn'}, \quad (3)$$

where $\varepsilon_n(k_0)$ is the energy of the nth band at k_0, and $p_{k_0}^{nn'}$ is the transition matrix element between the Bloch states with the same k_0 and different band indices:

$$p_{k_0}^{nn'} = \langle \phi_{nk_0} | \hat{p} | \phi_{n'k_0} \rangle. \quad (4)$$

We note here that Eq. (3) for a single k_0 channel is simply the TDSE for a multilevel system interacting with a laser field, so that the solid dynamics can be constructed as an ensemble of independent multilevel systems.

To calculate the HHG signal we need the coherent part of the current, which is

$$j_{k_0}(t) = -[\langle \psi_{k_0}(t) | \hat{p} | \psi_{k_0}(t) \rangle + A(t)]$$

$$= -\left[\text{Re} \left[\sum_{n,n'} C_{nk_0}^*(t) C_{n'k_0}(t) p_{k_0}^{nn'} \right] + A(t) \right] \quad (5)$$

in each k_0 channel. In principle, we need to consider all possible k_0 in the first Brillouin zone and calculate the total current as

$$j(t) = \int_{k_0 \in \text{BZ}} j_{k_0}(t) dk_0. \quad (6)$$

In this paper, however, we restrict our study to the single excitation channel, $k_0 = 0$, corresponding to a maximally (spatially) delocalized Bloch state at the high symmetry point Γ of the band structure. In our 1D model, as in many direct band-gap materials, the transition matrix element between the VB and the CB is maximized at $k_0 = 0$. This is, in particular, true in solid argon, which we use as an example below. This means that the electron at $k_0 = 0$ has the highest excitation probability to the higher conduction bands. One therefore expects the largest contribution to the highly nonlinear HHG yield to originate at $k_0 = 0$, as has indeed been verified in calculations incorporating the 3D band structure [27], at moderate intensities. Moreover, for the purposes of this work, using a single k_0 channel allows us a straightforward extension beyond a two-band model which was shown to be necessary to

reproduce the multiple harmonic plateaus observed in recent experiments [20,26]. With this initial condition, the dynamics of the solid is equivalent to that of a multilevel system, where the levels are the Bloch states for the different bands at a specific k_0, and the transition matrix elements are those between the Bloch states of the same k_0 in different bands.

III. HIGH-HARMONIC GENERATION IN A TWO-LEVEL SYSTEM

In this section, we review HHG in the simplest multilevel system—the two-level system. The HHG process in a two-level system has been studied extensively before, mostly in the context of atomic states with a coupling specified in terms of the electric field, in the length gauge [33–46]. Our two-level system originates in a two-band solid and consists of Bloch states in two different bands but with the same k_0 that are coupled by the vector potential as shown in Eq. (3). The Hamiltonian for our laser-driven two-level system can then be written as

$$H = \begin{pmatrix} \omega_1 & \mu A(t) \\ \mu A(t) & \omega_2 \end{pmatrix}, \quad (7)$$

where the two levels correspond to the valence and conduction bands at $k_0 = 0$. $\mu = p_{k_0=0}^{vc}$ is the transition matrix element between these two Bloch states, and ω_1 and ω_2 are the energy of the highest valence band and the lowest conduction band, respectively. Their energy difference is defined as $\omega_0 = \omega_2 - \omega_1$, which is the band gap at $k_0 = 0$. In our numerical calculations we use a laser pulse with a central frequency ω. The pulse is derived from the vector potential $A(t)$ that has a $\cos^4$ envelope:

$$A(t) = A_0 \cos^4\left(\frac{\omega t}{2n}\right) \cos(\omega t), \quad -\frac{n\pi}{\omega} \leqslant t \leqslant \frac{n\pi}{\omega}. \quad (8)$$

A_0 is the peak vector potential and n is the total number of cycles used in the calculation. It is also useful to define the peak Rabi frequency Ω_0 and the time-dependent Rabi frequency $\wp(t)$:

$$\Omega_0 = \mu A_0, \quad (9)$$

$$\wp(t) = \mu A(t). \quad (10)$$

Then the Hamiltonian for this two-level model can be written as

$$H = \begin{pmatrix} \omega_1 & \wp(t) \\ \wp(t) & \omega_2 \end{pmatrix}. \quad (11)$$

A typical harmonic spectrum from a strongly driven two-level system is shown in Fig. 1(a), where the two-level energy separation is $\omega_0 = 1$ a.u., the laser frequency is $\omega = 0.1$ a.u., the Rabi frequency is $\Omega_0 = 2$ a.u., and the total number of cycles in the pulse is $n = 11$, which yields a FWHM duration of about three cycles for the envelope we are using. The spectrum exhibits a perturbative regime (photon energies between ω and 9ω), a plateau regime (photon energies between 9ω and 41ω), and a cutoff regime with a fast decline (photon energies $>41\omega$).

For the parameters used in Fig. 1 the HHG process in the two-level system can best be described using the time-dependent adiabatic states of the system, which are the
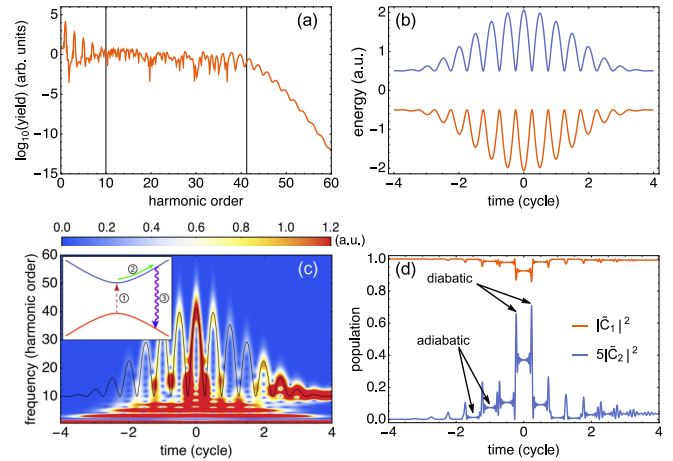

FIG. 1. (a) Harmonic spectrum for a two-level system, with parameters $\omega_0 = 1$ a.u., $\Omega_0 = 2$ a.u., and $\omega = 0.1$ a.u. (b) Adiabatic-state energies as a function of time. Avoided crossings are formed at the zeros of the vector potential. (c) Wavelet transform of the time-dependent current, corresponding to the emission time of the harmonics. The thin black line indicates the energy difference between the adiabatic states in (b). Inset: Three-step picture for the HHG process near an avoided crossing (see text). (d) Population in the two adiabatic eigenstates.

instantaneous eigenstates of the time-dependent Hamiltonian in Eq. (11) [37,38,40]. For the full description of the adiabatic basis, see Appendix A. Diagonalizing the time-dependent Hamiltonian in Eq. (11) we get the time-dependent energies of the adiabatic states,

$$\mathcal{E}_\pm(t) = \pm\sqrt{\wp^2(t) + \left(\frac{\omega_0}{2}\right)^2}, \quad (12)$$

which are shown in Fig. 1(b). For our choice of parameters, $\Omega_0 = 2\omega_0$, the dressed-state energies $\mathcal{E}_\pm(t)$ almost trace the magnitude of the vector potential $\pm|A(t)|$. Their separation is maximized at the peaks of the vector potential and minimized at the zeros of the vector potential, where the two adiabatic states form avoided crossings.

To illustrate the usefulness of the adiabatic basis, we explore the time-frequency properties of the two-level harmonics in Fig. 1(c), which shows the wavelet transform of the time-dependent current, using a Gabor wavelet, $g(t) = \frac{1}{4\sqrt{\pi}} e^{-\frac{t^2}{2} + 10it}$ [47]. The wavelet transform is similar to a time-limited, sliding-window Fourier transform and reveals the emission time of the harmonics. The thin curve overlaid on top is the energy difference between the two adiabatic states $\mathcal{E}_+(t) - \mathcal{E}_-(t)$. We see that the two-level harmonic emission process involves two symmetric "paths," and the emission time of each path agrees very well with the adiabatic-state energies.

The time evolution of the excited-state population is also most easily understood in the adiabatic-state basis, as shown in Fig. 1(d). In this basis, the population evolution can be separated into *adiabatic* and *diabatic* processes, as indicated by the arrows in Fig. 1(d). The adiabatic process manifests itself as the dressed level population's staying the same, while in the diabatic process the population changes abruptly. The diabatic processes take place at the zeros of the vector potential

when the two states form avoided crossings and the time-dependent transition matrix element between the adiabatic states is greatly peaked [see Eq. (A12) in Appendix A]. Between the avoided crossings the system evolves almost adiabatically, so the populations in the two adiabatic states stay almost the same. This adiabatic evolution corresponds to rapid oscillations in the bare-state populations (not shown), and the resulting nonlinear current is responsible for the high harmonics generated between the zeros of the vector potential as shown in Fig. 1(c).

From the above analysis of the time-frequency properties of the harmonics and the population evolution in the adiabatic states, a three-step picture emerges for HHG in the two-level system in the adiabatic basis, as shown in the inset in Fig. 1(c). The inset shows the enlargement of an avoided crossing in Fig. 1(b). In the first step, the population tunnels through the avoided crossings from the lower adiabatic state to the upper adiabatic state. In the second step, the population in the adiabatic states evolves adiabatically, gaining a phase proportional to their time-dependent energy separation. In the final step, the coherence between the adiabatic states generates high harmonics with energies corresponding to the instantaneous energy separation between the two adiabatic states. The lowest harmonic generated in this process is at the bare-state two-level energy difference,[1] and the highest harmonic is generated at the largest energy difference between the two dressed states [37,38],

$$E_{\text{low}} = \omega_0, \tag{13}$$

$$E_{\text{cutoff}} = 2\sqrt{\Omega_0^2 + \left(\frac{\omega_0}{2}\right)^2}. \tag{14}$$

The lowest and the highest harmonics predicted by these formulas are indicated by the vertical lines in Fig. 1(a) and can be seen to agree very well with the extent of the plateau region.

The three-step picture of HHG in a two-level system works well when the diabatic interactions are short compared to the adiabatic evolution, so that the "diabatic tunneling" and the "adiabatic following" can be separated in time. The condition for the well-separated adiabatic and diabatic processes can be written as a "crossing parameter," $R = \omega_0/2\Omega_0$ [38]. For a high intensity and small two-level separation such that $R \ll 1$, the adiabatic and diabatic processes are well separated and thus the three-step picture works very well, whereas for a low intensity and large two-level separation such that $R \gg 1$, the adiabatic and diabatic processes are not well separated and the three-step picture may not apply. For our parameters in Fig. 1, $R = 0.25$ and the adiabatic and diabatic description works very well as expected.

In the two-level model of harmonic generation, the cutoff is determined by the maximum energy difference between the adiabatic states [see Eq. (14)]. For intense fields, the cutoff is approximately linear with the field strength, i.e., $E_{\text{cutoff}} \approx 2\Omega_0$. Figure 2(a) shows the field dependence of the

---

[1]Harmonics with lower energies are generated in a perturbative process, with strengths that decrease rapidly with order.
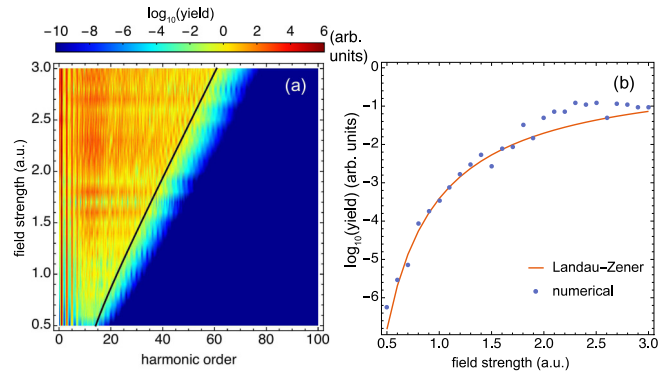

FIG. 2. (a) Evolution of the harmonic spectrum as a function of the peak field strength. The solid line indicates the prediction for the cutoff from Eq. (14). As the Rabi frequency exceeds the two-level energy, the cutoff is approximately linear with the field strength. (b) The strength of the harmonic plateau (blue dots) agrees with the prediction of Landau-Zener tunneling (solid red line) very well.

harmonic spectrum, overlaid on top of which is the cutoff predicted from Eq. (14). The cutoff formula Eq. (14) works very well. Since the harmonics are generated by the coherence between the adiabatic states, the harmonic strength is then determined by the population at the adiabatic states, which is directly related to the tunneling rate between the adiabatic states at the avoided crossings. This tunneling rate can be calculated using the Landau-Zener tunneling formula near an avoided crossing [38],

$$P = \alpha \exp\left(-\frac{\pi\omega_0^2}{4\omega\Omega_0}\right), \tag{15}$$

where α is a scaling factor. The dots in Fig. 2(b) show the yield of the harmonics in the plateau (measured by the strength of the cutoff harmonic) for different electric-field values [defined as $E(t) = -\dot{A}(t)$]. The solid line shows the prediction from Eq. (15) with $\alpha = 10$. We can see that Eq. (15) works well in predicting the intensity of the plateau.

IV. HHG IN A MULTILEVEL SYSTEM

In this section we expand from a two-level system to a multilevel system. We begin with a four-level system, again formed by the Bloch states of a 1D model solid at $k_0 = 0$. Our model solid has a Mathieu-type periodic potential $V(x) = -V_0[1 + \cos(2\pi x/a_0)]$, with $V_0 = 0.37$ a.u. and lattice constant $a_0 = 8$ a.u. This potential conveniently has a band structure that can be expressed in terms of Matheiu characteristic values [48]. The harmonic spectrum from this solid system can be calculated by solving the TDSE in the Bloch-state basis and the resulting harmonic spectrum exhibits multiple plateaus, as described in [26]. The energies and coupling matrix elements for the lowest five Bloch states at $k_0 = 0$ can be calculated by solving the time-independent Schrödinger equation and are listed in Table I. For our four-level system, we discard the lowest-energy Bloch state and use the second-lowest state as the valence band. Table I also shows that the coupling between the four levels predominantly

TABLE I. Energies and transition matrix element for the first five Bloch states at $k_0 = 0$ of the 1D solid. For the four-level system, we use the Bloch state from level 1 to level 4 (see text).

	Transition matrix element (a.u.) [Eq. (4)]					
			Level			
Level	0	1	2	3	4	Energy (a.u.)
0	0	0.41	0	0.03	0	−0.526
1	0.41	0	0.70	0	0.14	−0.098
2	0	0.70	0	0.18	0	0.056
3	0.03	0	0.18	0	1.55	0.878
4	0	0.14	0	1.55	0	0.880

takes place in a stepwise manner, since the coupling matrix elements between neighboring levels are much larger than across multiple levels.

The harmonic spectrum from the four-level system, driven by a 3.2 μm laser with a field strength of $E_0 = 4.1 \times 10^{-3}$ a.u. is shown in Fig. 3(a). We note that retaining more Bloch states in the TDSE calculation does not change the harmonic spectrum for a range of field strengths (see [26]). The spectrum exhibits a characteristic two-plateau structure, where each plateau has an onset energy and a cutoff. The mechanism for this two-plateau structure can be understood by extending the three-step picture discussed for the two-level system in the previous section. The time-dependent energies of the adiabatic states for the four-level system are plotted in Fig. 3(b). The adiabatic states form two pairs of two closely coupled states, resembling the adiabatic states of our two-level system in Fig. 1(b). The dynamics in the four-level system can then be understood similarly to that in the two-level system, where harmonics are generated by the transitions between the adiabatic states, except now we can have transitions from all three higher adiabatic states to the lowest adiabatic state.
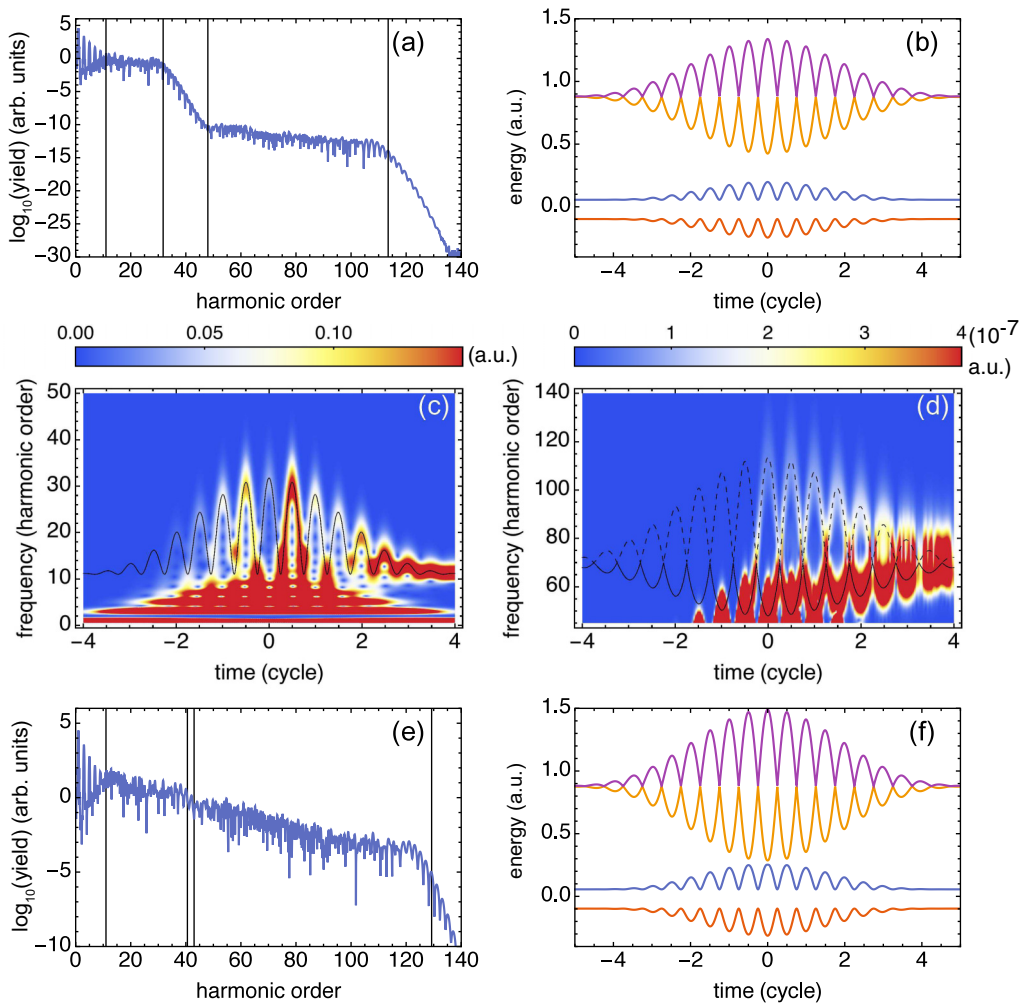

FIG. 3. (a) HHG spectrum from a four-level system, with field strength $E_0 = 4.1 \times 10^{-3}$ a.u. The harmonic spectrum has two plateaus. Solid lines indicate the predictions from Eqs. (17)–(19) for the lowest and cutoff energies of the two plateaus. (b) Energy of the adiabatic states as a function of time. (c) Wavelet transform of the time-dependent current in the energy range of the first plateau. The overlying solid line represents the energy difference between the first and the second adiabatic states. (d) Same as (c) but in the range of the second plateau. The solid line indicates the energy difference between the first and the third adiabatic states, whereas the dashed line indicates the energy difference between the first and the fourth adiabatic states. (e, f) The same as (a) and (b) but with field strength $E_0 = 5.5 \times 10^{-3}$ a.u. At this field strength, the second plateau merges onto the first plateau.
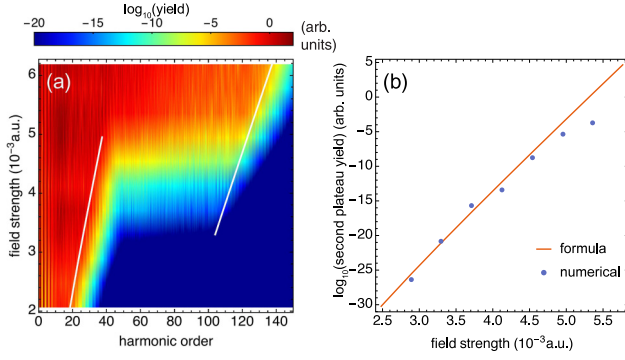
FIG. 4. (a) Harmonic spectrum for a four-level system as a function of the field strength. The cutoffs predicted from Eq. (17) and Eq. (19) are indicated by white lines (b) The intensity of the second plateau (blue dots) agrees very well with the prediction from Eq. (24) (solid red line).

Figure 3(c) shows the wavelet transform of the time-dependent current in the energy range of the first plateau, which describes the emission time of the harmonics in the first plateau. The overlain black line is the energy difference between the first and the second adiabatic states $\mathcal{E}_2(t) - \mathcal{E}_1(t)$. Figure 3(d) shows the same wavelet transform but in the second plateau region. The dashed and solid black lines are the energy differences between the third, fourth, and first adiabatic states, respectively. We can see that the adiabatic energies agree very well with the harmonic emission times in both the first and the second plateaus, suggesting that this adiabatic-state description of the four-level dynamics works very well. Similarly to the two-level system, the allowed harmonics are then determined by the allowed energy range of the adiabatic states. We defined the energies of the adiabatic states at the peak of the vector potential as $\tilde{\mathcal{E}}_n$, where n goes from 1 to 4. Then the first plateau is due to the transition between the first and the second adiabatic states, which has start and cutoff energies of

$$E_{\text{low}}^{(1)} = \omega_2 - \omega_1, \tag{16}$$

$$E_{\text{cutoff}}^{(1)} = \tilde{\mathcal{E}}_2 - \tilde{\mathcal{E}}_1. \tag{17}$$

Similarly, the second plateau is due to the transition from the third and fourth adiabatic states to the first adiabatic state, which has start and cutoff energies of

$$E_{\text{low}}^{(2)} = \tilde{\mathcal{E}}_3 - \tilde{\mathcal{E}}_1, \tag{18}$$

$$E_{\text{cutoff}}^{(2)} = \tilde{\mathcal{E}}_4 - \tilde{\mathcal{E}}_1. \tag{19}$$

These four energies are indicated by the vertical lines in Fig. 3(a). We can see that the beginning and end of the two plateaus from these formula agree very well with the plateau spans that can be seen in the harmonic spectrum. The agreement between the predicted cutoff energies and the numerical results is very good for a range of intensities, as shown in the intensity scan in Fig. 4(a).

We turn next to the relative strength of the two harmonic plateaus in the four-level system. Similarly to the two-level system, the intensities of the harmonic plateaus in the four-level

system are determined by the population of the adiabatic states, which in turn are determined by the tunneling rates between them. As reported in Table I, the 1–2 and 3–4 couplings are much stronger than the 2–3 coupling, which means that the four-level system can be thought of as two weakly coupled two-level systems. This means that the intensity of the first plateau in the four-level system will be proportional to the tunneling rate P_{12} between the first and the second adiabatic states, given by the Landau-Zener rate [see Eq. (15)],

$$I_{\text{1st}} \propto P_{12} = \exp\left(-\frac{\pi(\omega_2 - \omega_1)^2}{4\omega\mu_{12}A_0}\right). \tag{20}$$

The intensity of the second plateau is more complicated. Since the four levels are coupled in a stepwise manner, population transfer between the adiabatic states also happens in a stepwise manner, and the population of the fourth adiabatic state results from stepwise tunneling from state 1 to state 2, state 2 to state 3, and state 3 to state 4. The total tunneling rate between 1 and 4 can be written as the product of these three tunnelings:

$$I_{\text{2nd}} \propto P_{12} \times P_{23} \times P_{34}. \tag{21}$$

Since the two two-level systems are almost independent, the tunneling rates P_{12} and P_{34} are of the Landau-Zener form. The 2–3 tunneling process is different because levels 2 and 3 are only weakly coupled to each other and there is no avoided crossing between them for low field strengths. The 2–3 tunneling will take place predominantly when the two levels have been pushed as close together as possible due to their respective interactions with levels 1 and 4, which happens at the peaks of the vector potential. This tunneling event is therefore not field driven in the same way that the Landau-Zener tunneling is. Instead, this transition amplitude can be calculated in analogy with the WKB calculation of the reflection of a wave passing over a potential barrier [49]. The minimum energy difference between the levels (which happens at the peaks of the vector potential) is analogous to the energy of the wave above the top of the barrier in the WKB calculation, and the width of the barrier is analogous to the time the levels spend close to each other, which is set by the laser period. We thus expect the transition probability to decrease exponentially with the energy difference [49],

$$P_{23} = \exp[-\beta(\tilde{\mathcal{E}}_3 - \tilde{\mathcal{E}}_2)], \tag{22}$$

where $\tilde{\mathcal{E}}_3 - \tilde{\mathcal{E}}_2$ is the energy difference between the two adiabatic states at the peak of the vector potential and β is a constant.[2] This minimum energy difference can be approximated as

$$\tilde{\mathcal{E}}_3 - \tilde{\mathcal{E}}_2 \approx (\omega_3 - \omega_2) - (\mu_{12} + \mu_{34})A_0, \tag{23}$$

corresponding to the field free energy difference, minus the amount the two levels have been pushed together by their respective interactions with levels 1 and 4.

Our analysis of the stepwise tunneling process that populates the fourth adiabatic state leads to an intensity of the

---

[2]We note that β should be inversely proportional to the frequency, although our calculations are all done at the same wavelength.
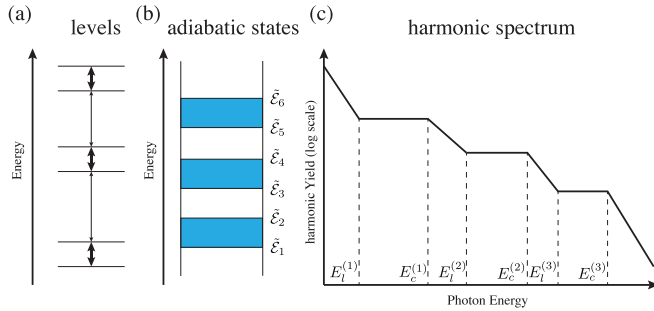
FIG. 5. (a) Schematic of a multilevel system where levels are coupled in pairs. (b) The energies of the adiabatic states form allowed regions indicated by the blue area. (c) Schematic of the multiplateau structure from this multilevel system. The beginning and end of each plateau are determined by the bounds of the allowed energy regions, as in Eqs. (17) and (19).
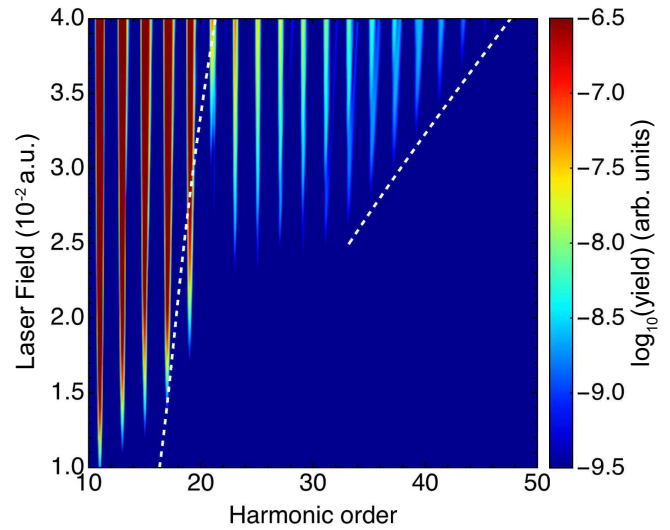

FIG. 6. Intensity-dependent harmonic spectra for the four-level model for solid argon. Dashed lines indicate the cutoff prediction from Eq. (17) and Eq. (19).

second plateau that, according to Eq. (21), is proportional to

$$
I_{2\text{nd}} \propto \exp\left[-\frac{\pi(\omega_2 - \omega_1)^2}{4\omega \mu_{12} A_0} \right]
$$
$$
\times \exp[-\beta(\omega_3 - \omega_2 - (\mu_{12} + \mu_{34})A_0)]
$$
$$
\times \exp\left[-\frac{\pi(\omega_4 - \omega_3)^2}{4\omega \mu_{34} A_0} \right]. \tag{24}
$$

Figure 4(b) shows the comparison between the numerically calculated harmonic intensity of the second plateau and that from Eq. (24) with the scaling parameter $\beta = 140$. We see that they agree very well. At field strengths $E_0 \geqslant 5.5 \times 10^{-3}$ a.u., the two results start to deviate. This is because at fields higher than this, the adiabatic states 2 and 3 will cross each other in energy, and a simple exponential tunneling rate will break down. Furthermore, when $\tilde{\mathcal{E}}_2 \approx \tilde{\mathcal{E}}_3$ the population very easily tunnels between the second and the third adiabatic states, and as a consequence, the second plateau will rise to a point where it almost merges with the first plateau. This can be seen in the harmonic spectrum shown in Fig. 3(e), calculated at a field strength of $E_0 = 5.5 \times 10^{-3}$ a.u.

In the four-level system considered above, the harmonics are generated from two pairs of coupled adiabatic states. This picture of high-harmonic generation can be generalized to systems with more than four levels, as illustrated in Fig. 5. Figure 5(a) shows a multilevel system in which the levels are coupled in a stepwise manner. In particular, the levels in the multilevel system form pairs of strongly coupled two-level systems. The adiabatic states of this chain of multilevel system then form blocks of allowed energies, as indicated by the blue region in Fig. 5(b). The harmonic spectrum generated by this multilevel system has multiple plateaus, as shown in Fig. 5(c). The beginning and end of each plateau correspond to the lower and higher bounds for the corresponding block of adiabatic energies. More generally, if the multilevel system is not strongly coupled in pairs of states as we have considered here, the harmonic spectrum can exhibit even more plateaus. As an example, in the four-level system considered in Fig. 3 levels 3 and 4 are near degenerate and very strongly coupled to each other. A four-level system in which these levels were less degenerate would lead to harmonic spectra with three

plateaus, corresponding to transitions from the second, third, and fourth adiabatic levels to the lowest level, with cutoff energies each determined by the maximum adiabatic-state energy separations.

Finally, we end this section by returning to the experimental observations of multiple plateaus in solid argon and krypton as reported in [20]. The calculations describing HHG in solid argon in [20] were based on a multilevel model similar to that described above, except the energy levels and transition matrix elements originated in a density functional theory (DFT) calculation of the 3D argon band structure. The energies of the four lowest bands at the Γ point in solid argon are 0, 14, 20, and 29 eV, and we found that including these four levels was sufficient to get converged harmonic spectra. We used the experimental observations of the cutoff energies and relative strengths of the first and second plateaus to adjust the transition matrix elements between the different levels from the DFT predictions. In particular, the experiment showed a rapid increase in the secondary plateau with the intensity, so that it nearly matched the strength of the primary plateau, similar to the situation discussed in the context of Fig. 3(e). Also, the experiment demonstrated that the difference between the two cutoff energies (approximately 25 and 33 eV, respectively, at an intensity of 20 TW/cm^2 and a wavelength of 1333 nm) was relatively modest given the separation between levels 2, 3, and 4. We found the best agreement with the experimental results when using stepwise coupling matrix elements of approximately equal strength (as opposed to the DFT prediction of a weak coupling between level 2 and level 3) so that the relatively strong coupling between level 2 and level 3 both acts to cap the cutoff energy of the primary plateau and gives rise to a strong secondary plateau as discussed above. The resulting intensity-dependent spectra are shown in Fig. 6. We note that although the third plateau, due to the transitions between level 4 and level 1, is so weak it is not visible on the scale shown in the figure, the fourth level plays an important role in capping the cutoff energy of the secondary plateau.
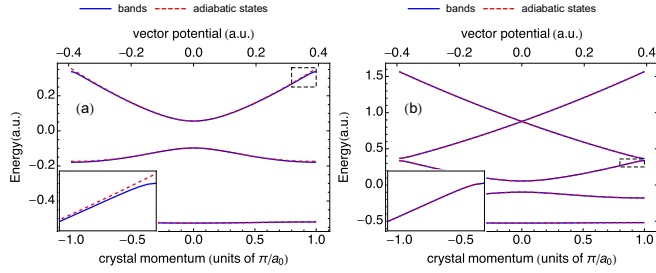
FIG. 7. Comparison of the band structure (solid blue lines; bottom axis) and the energy of the adiabatic states vs the vector potential (dashed red lines; top axis) for (a) a three-level and (b) a five-level system. Insets: Zoom-ins of the region near the edge of the third band, indicated by boxes.

V. SEMICLASSICAL PICTURE OF HHG IN SOLIDS

In Sec. II we showed that the electron dynamics in solids can be formulated as the dynamics in a multilevel system, and we have provided a three-step picture in Secs. III and IV for harmonic generation in the multilevel system. We now return to the study of the connection between a model solid and a multilevel system. We show that this connection provides a semiclassical picture for the harmonic generation process by delocalized electrons in a solid. In Appendix C we show that this picture can also be arrived at via applying the strong-field approximation (SFA) [6,8,50–52] to the dynamics of strongly driven Bloch electrons.

We start by considering the evolution of the adiabatic-state energies with the field strength. As discussed in Sec. IV the maximum difference between these energies at a given field strength will determine the cutoff energies of the different plateaus. Figure 7(a) shows the energies of the adiabatic states for a three-level system as functions of the driving vector potential (dashed red lines; vector potential along top axis). We compare these to the band structure of the three lowest bands in our model solid, i.e., we plot the energies of the bands as functions of the crystal momentum (solid blue lines; crystal momentum along the bottom axis). We see that the energies of the adiabatic states, when driven by a laser field with a vector potential A_0, map out the band structure very well when we assign a value of $k = A_0$ to the crystal momentum.

The origin of this agreement can be understood by considering the Houston-state basis for the solid, which is related to the Bloch-state basis via a unitary transformation (see [26] for details). The Houston states are constructed as the instantaneous eigenstates of the time-dependent Hamiltonian, which includes both the crystal potential and the field in the dipole approximation. The Houston states are thus the adiabatic states by definition. They are characterized by a time-dependent momentum $k(t) = k_0 + A(t)$, where k_0 is the value of the crystal momentum in the absence of a field (corresponding to the Bloch state with $k = k_0$). The energies of the Houston states $\tilde{\varepsilon}_n(t)$ are simply the energies of the Bloch states at the crystal momentum that corresponds to the vector potential [26,32],

$$\tilde{\varepsilon}_n(t) = \varepsilon_n(k(t)) - \tfrac{1}{2}A^2(t), \quad \text{with} \quad k(t) = k_0 + A(t), \quad (25)$$
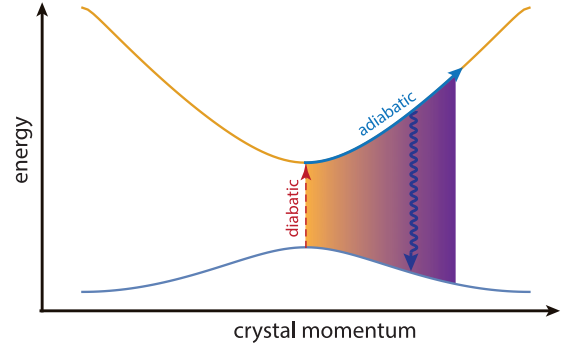

FIG. 8. Schematic of the momentum-space three-step picture for harmonic generation in solids. In the first step, the valence electron tunnels through the band gap. In the second step, the electron wave function evolves adiabatically in the valence and conduction bands. In the final step, the coherence between the valence and the conduction band states leads to the emission of radiation with energies corresponding to the instantaneous energy difference between the dressed valence and conduction bands.

where the constant term comes from the fact that the Bloch and Houston Hamiltonians differ by a $\tfrac{1}{2}A^2$ term (see [26]).

An important implication of Eq. (25) is that the band structure at all k is encoded at $k_0 = 0$ (or any other initial k_0) through the energies of the Bloch states and transition matrix elements between them. This means that as long as our multilevel system is constructed from the energies and coupling strengths of our model solid, its evolution with the vector potential is in fact equivalent to the evolution of the Houston states and should indeed yield the band structure. In fact, the Houston description is the adiabatic-state description of the dynamics in the Bloch-state basis. A complete proof of this relationship can be found in Appendix B.

We note that the agreement between the adiabatic states and the band structure improves with the inclusion of more levels in the multilevel model. This is illustrated in the comparison between Fig. 7(a) and Fig. 7(b), in particular, as magnified in the insets. In a multilevel system, the energies of the adiabatic states are determined by their interactions both with the laser field and with each other. The former leads to an approximately linear variation with field strength, whereas the latter leads to avoided crossings. In a multilevel description, it is the avoided crossings with higher-lying levels that allow lower-lying levels to "turn over" at high field strengths and thus mimic the band structure at the edge of the Brillouin zone, as shown in the inset in Fig. 7(b). In contrast, in the absence of higher-lying levels, the adiabatic energy will continue to increase linearly as shown in the inset in Fig. 7(a).

Another important implication of the result in Fig. 7 and the energy relationship described in Eq. (25) is that it offers a picture of how the harmonic generation process for Bloch electrons in solids takes place in three steps, similar to the well-known three-step model for harmonic generation in gases. This picture is illustrated in Fig. 8 for a two-band system. In the first step, which in time corresponds to the zeros of the vector potential, a part of the delocalized electron wave packet diabatically tunnels through the band gap into the conduction band via Landau-Zener tunneling. In the

second step, the valence and conduction band wave functions both evolve adiabatically, accumulating phases according to their instantaneous energies. In the third step, the coherence between the conduction band and the valence electron leads to the emission of radiation with an energy corresponding to the instantaneous band gap. The third step leads to emission during the entire optical half-cycle, from one 0 of the vector potential to the next, where each energy below the cutoff is emitted at two different times as the vector potential increases and decreases, as also shown in Fig. 3(c). The cutoff energy is determined by the instantaneous band gap at the peak of the vector potential,

$$E_{\text{cutoff}} = \varepsilon_c(A_0) - \varepsilon_v(A_0), \tag{26}$$

and therefore cannot exceed the maximum band gap of the two-band system. In a multiband system, this generalizes to the conclusion that the cutoff energies of each plateau will be limited by the maximum separation between the VB and the uppermost CB responsible for that plateau,

$$E_{\text{cutoff}}^n = \varepsilon_{nc}(A_0) - \varepsilon_v(A_0), \tag{27}$$

as illustrated in Fig. 5.

The cutoff formula above, and its limit on the maximum band gap in the case of a two-band system, recovers the cutoff formula discussed by Vampa and collaborators in [28]. In [28], a *real-space* three-step picture of HHG in solids is discussed in terms of localized electron and hole separation, acceleration, and recollision. The laser pulse generates electron-hole pairs and they travel in opposite directions in space and then recombine as the vector potential changes sign. A similar real-space picture was also presented by Higuchi *et al.* in [24], where the dynamics is described in terms of (localized) Wannier states and the recollision is described in terms of the electron recombination to neighboring cores. In contrast, in this paper we discuss a *momentum space* three-step picture of the HHG process, in terms of adiabatic and diabatic evolution of the initial (delocalized) Bloch state. The harmonics in this picture comes from the coherence between the one-electron VB and CB Bloch states.

VI. SUMMARY

In this paper, we have investigated HHG in a multilevel system and discussed how such a model can be used to describe HHG in bulk solids, a subject that is currently of great interest in the ultrafast community [14–20]. We have shown that a driven multilevel system generally gives rise to harmonic spectra exhibiting multiple plateaus and that the cutoff energies and relative strengths of each plateau can be calculated using simple formulas. We have discussed how the strong-field dynamics is best described in the adiabatic (dressed)-state basis for the multilevel system. In this basis, the HHG process happens via tunneling of the population from a lower to an upper state, followed by evolution of the population in the excited state and, finally, transition back to the ground state. This means that the cutoff energies of each plateau at a given field strength are simply determined by the maximum energy difference between the field-dressed upper and lower adiabatic states. The strength of each plateau, and, in particular, its dependence on the field strength, can

be calculated considering a sequence of tunneling events. In a four-level system in which the states are strongly coupled in pairs, the secondary plateau is due to transitions from the third and fourth adiabatic states to the first adiabatic state, where the highest state is reached via tunneling from 1 to 2, from 2 to 3, and, finally, from 3 to 4. We have also discussed how detailed knowledge of driven multilevel dynamics can be used in reverse to draw conclusions from experimental HHG results. We used the recent example of HHG in solid argon, in which the appearance of multiple plateaus and their relative extents and strengths were used as an indication of the contributions and relative couplings of several conduction bands [20].

We have also shown that if the multilevel system originates in the $k = 0$ component of the band structure of a periodic system, the adiabatic states of the multilevel system will map out the entire band structure as the field strength is increased. This means that the maximum cutoff energies of each plateau will be limited by the band structure: The highest photon energy emitted in a given plateau will be limited by the largest energy separation in the Brillouin zone between the VB and the CB, which is responsible for that particular plateau. This could potentially be used to map out the band structure, including the high-lying bands in the solid, by careful measurements of how different cutoff energies scale with the intensity, in analogy with our discussion of solid argon above. For materials that have very different band structures along different crystal orientations, one can also expect to see crystal-orientation-dependent harmonics and mapping-out of the 3D band structure by measurements of how different cutoff energies scale with the intensity along different crystal orientations.

The correspondence between the adiabatic states and the band structure also leads naturally to a semiclassical, three-step picture for HHG by Bloch electrons in a solid: In the first step, a part of the delocalized electron wave packet diabatically tunnels through the band gap into the conduction band via Landau-Zener tunneling. In the second step, the VB and CB wave functions both evolve adiabatically, accumulating phases according to their instantaneous energies. In the third step, the coherence between the conduction band and the valence electron leads to the emission of radiation with an energy corresponding to the instantaneous band gap. The harmonic emission is thus chirped in time, at the subcycle level, similarly to what happens in gas-phase HHG.

This momentum-space picture can potentially also shed light on the measured ellipticity dependence of harmonics in solid argon as reported in [20], where the yield of the harmonics in the plateau was found to decrease exponentially with the ellipticity, similarly to what is found in gas-phase argon. In a linearly polarized field, the VB-to-CB tunneling of the electron takes place twice each laser cycle around the Γ point when the electron traverses the Brillouin-zone center. The intensity of the harmonics in the plateau is then determined by this tunneling rate around the Γ point. For a circularly polarized field, the electron will rotate around the Γ point in momentum space, without ever getting close to the Γ point, thus the tunneling rate is greatly suppressed. The details of the ellipticity dependence of HHG in solids will be studied in a future paper.

APPENDIX A: ADIATIC-BASIS FORMALISM

In this Appendix we describe the formalism for a multilevel system in the adiabatic basis. The TDSE reads

$$i \, |\dot{\psi}(t)\rangle = H(t) \, |\psi(t)\rangle \,, \tag{A1}$$

and the Hamiltonian is

$$H(t) = H_0 + A(t)\hat{p}, \tag{A2}$$

where H_0 is the laser free Hamiltonian, $A(t)$ is the vector potential, and $\hat{p}$ is the dipole operator in momentum space. The adiabatic states are the instantaneous eigenstates of the time-dependent Hamiltonian,

$$H(t) \, |\phi_n(t)\rangle = \mathcal{E}_n(t) \, |\phi_n(t)\rangle \,, \tag{A3}$$

where $|\phi_n(t)\rangle$ is an adiabatic state and $\mathcal{E}_n(t)$ is its energy. Since the adiabatic states are the instantaneous eigenstates of the time-dependent Hamiltonian, they are time dependent themselves. However, at any given time t they are orthogonal and form a complete basis set:

$$\langle \phi_n(t)|\phi_m(t)\rangle = \delta_{nm}. \tag{A4}$$

This means that the time-dependent wave function $|\psi(t)\rangle$ can be expanded in the adiabatic basis as

$$|\psi(t)\rangle = \sum_n \tilde{C}_n(t) \, |\phi_n(t)\rangle \,, \tag{A5}$$

where $\tilde{C}_n(t)$ is the amplitude of the adiabatic state $|\phi_n(t)\rangle$. In the following, we leave out the explicit indication of time dependence and write $|\phi(t)\rangle$ and $\tilde{C}_n(t)$ as $|\phi\rangle$ and $\tilde{C}_n$, respectively, for brevity. Substituting the wave function into the Schrödinger equation, we have

$$i \sum_n \dot{\tilde{C}}_n \, |\phi_n\rangle + i \sum_n \tilde{C}_n \, |\dot{\phi}_n\rangle = \sum_n \tilde{C}_n H \, |\phi_n\rangle \,. \tag{A6}$$

Projecting onto one of the adiabatic states, we obtain the following equation:

$$i\dot{\tilde{C}}_n + i \sum_m \tilde{C}_m \langle \phi_n|\dot{\phi}_m\rangle = \tilde{C}_n \mathcal{E}_n. \tag{A7}$$

To calculate the term $\langle \phi_n|\dot{\phi}_m\rangle$, we take the derivative of Eq. (A3) and project onto one of the adiabatic states:

$$\langle \phi_n|\dot{H}|\phi_m\rangle + \mathcal{E}_n \langle \phi_n|\dot{\phi}_m\rangle = \dot{\mathcal{E}}_m \delta_{mn} + \mathcal{E}_m \langle \phi_n|\dot{\phi}_m\rangle \,. \tag{A8}$$

This gives

$$\langle \phi_n|\dot{\phi}_m\rangle = \begin{cases} E(t)\frac{\langle \phi_n|\hat{p}|\phi_m\rangle}{\mathcal{E}_n - \mathcal{E}_m}, & m \neq n, \\ 0, & m = n, \end{cases} \tag{A9}$$

where $E(t) = -\dot{A}(t)$ is the electric field. Substituting Eq. (A9) and Eq. (A2) into Eq. (A7), we finally obtain the TDSE in the adiabatic basis,

$$i\dot{\tilde{C}}_n(t) = \sum_m [\mathcal{E}_m(t)\delta_{mn} - E(t)X_{mn}(t)]\tilde{C}_m(t), \tag{A10}$$

where

$$X_{mn}(t) = \begin{cases} i\frac{\langle \phi_m|\hat{p}|\phi_n\rangle}{\mathcal{E}_m - \mathcal{E}_n} & m \neq n \\ 0 & m = n \end{cases} \tag{A11}$$

indicates the transition matrix element between the adiabatic states. For a two-level system driven by a continuous wave $A(t) = A_0 \sin \omega t$, the transition matrix element has the form

$$X_{12}(t) = \frac{i\omega_0 \mu}{\omega_0^2 + 4A_0^2 \mu^2 \sin^2 \omega t}, \tag{A12}$$

where μ is the matrix element between Bloch states [Eq. (4)]. For the strongly driven case such that $\omega_0/2A_0\mu \ll 1$, $X_{12}(t)$ is small except near the zeros of the vector potential. This means that the population exchange between the adiabatic states happens only around the avoided crossings.

The time-dependent current in the adiabatic basis can be calculated as

$$j(t) = \langle \psi|\hat{p}|\psi\rangle \,. \tag{A13}$$

Substituting Eq. (A5) into the above equation, we can separate the current into two parts,

$$j(t) = j_{\text{intra}}(t) + j_{\text{inter}}(t), \tag{A14}$$

where j_{intra} and j_{inter} are the contribution from the dynamics in adiabatic states and between adiabatic states:

$$j_{\text{intra}}(t) = \sum_n \left| \tilde{C}_n \right|^2 \langle \phi_n|\hat{p}|\phi_n\rangle \,, \tag{A15}$$

$$j_{\text{inter}}(t) = \sum_{\substack{m,n \\ m \neq n}} \tilde{C}_m^* \tilde{C}_n \langle \phi_m|\hat{p}|\phi_n\rangle \,. \tag{A16}$$

In the context of strong-field dynamics in a solid, describing the dynamics in terms of the adiabatic states is equivalent to describing it in terms of the well-known Houston states since these are in fact the adiabatic states of the laser-driven solid [26]. The contributions from $j_{\text{intra}}(t)$ and $j_{\text{inter}}(t)$ are equivalent to the intraband and interband contributions, respectively.

APPENDIX B: ADIABATIC STATES IN A MULTILEVEL SYSTEM: CONNECTION TO THE BAND STRUCTURE

In this Appendix, we show that the energies of the adiabatic states for the multilevel system formed by the Bloch states at $k_0 = 0$ trace out the band structure of the solid. The Bloch states are the eigenstates of the laser-free Hamiltonian,

$$\left[\frac{\hat{p}^2}{2} + V(x) \right] |\phi_{nk_0}\rangle = \varepsilon_n(k_0) \, |\phi_{nk_0}\rangle \,. \tag{B1}$$

The adiabatic states for the multilevel system formed by the Bloch state at k_0 are the instantaneous eigenstates of the system when a vector potential A is applied,

$$\left[\frac{\hat{p}^2}{2} + V(x) + A\hat{p} \right] |\tilde{\phi}_{nk_0}\rangle = \mathcal{E}_n(A) \, |\tilde{\phi}_{nk_0}\rangle \,, \tag{B2}$$

where $\mathcal{E}_n(A)$ is the instantaneous energy of the nth adiabatic state and depends on the instantaneous vector potential A. The above equation can be written as

$$\left[\frac{(\hat{p}+A)^2}{2} + V(x) - \frac{A^2}{2}\right]|\tilde{\phi}_{nk_0}\rangle = \mathcal{E}_n(A)\,|\tilde{\phi}_{nk_0}\rangle. \quad \text{(B3)}$$

The Hamiltonians in Eqs. (B3) and (B1) differ by a constant. This means that the time-dependent wave functions for the adiabatic states and for the Bloch states are related by a phase factor and that the adiabatic-state energies can be written in terms of the band energies,

$$\mathcal{E}_n(A) = \varepsilon_n(k_0 + A) - \frac{A^2}{2}, \quad \text{(B4)}$$

so that the adiabatic-state energies map out the band structure.

APPENDIX C: STRONG-FIELD APPROXIMATION FOR SOLIDS

In this Appendix, we apply the SFA [50–52] to study strong-field dynamics in a two-band solid using a Bloch state as the initial condition. We show that the momentum-space three-step picture of HHG discussed in Sec. V also naturally follows from such an SFA treatment. We start from the TDSE,

$$i\frac{\partial}{\partial t}|\psi(t)\rangle = \left[\frac{(\hat{p}+A(t))^2}{2} + V(x)\right]|\psi(t)\rangle, \quad \text{(C1)}$$

where $V(x)$ is the periodic potential and $A(t)$ is the vector potential. The wave function can be expanded using the Houston states as

$$|\psi(t)\rangle = \sum_n a_{nk_0}(t)\,|\tilde{\phi}_{nk_0}(t)\rangle, \quad \text{(C2)}$$

where $|\tilde{\phi}_{nk_0}(t)\rangle$ are the Houston states and $a_{nk_0}(t)$ the expansion coefficients. Substituting Eq. (C2) into Eq. (C1), the TDSE has the form [26,32]

$$i\frac{\partial a_{nk_0}}{\partial t} = \sum_m \left[\varepsilon_n(k(t))\delta_{nm} - E(t)X_{nm}(k(t))\right]a_{mk_0}, \quad \text{(C3)}$$

where $E(t) = -\dot{A}(t)$ is the electric field and X_{nm} is the transition matrix elements between the Houston states. Note that Eq. (C3) has the same form as Eq. (A10), because the Houston states are the adiabatic states for the laser-dressed solid. For simplicity, we consider only the valence and conduction bands and limit ourselves to $k_0 = 0$; then the TDSE simplifies to

$$i\frac{\partial a_v}{\partial t} = \varepsilon_v(k(t))a_v - E(t)X_{vc}(k(t))a_c, \quad \text{(C4)}$$

$$i\frac{\partial a_c}{\partial t} = \varepsilon_c(k(t))a_c - E(t)X_{cv}(k(t))a_v, \quad \text{(C5)}$$

where $k(t) = k_0 + A(t)$. In analogy with the treatment in the SFA for gas-phase HHG, we assume that $|a_v| \approx 1$ so the VB

and CB amplitudes can be integrated analytically:

$$a_v(t) = \exp\left[-i\int_0^t \varepsilon_v(k(t'))dt'\right], \quad \text{(C6)}$$

$$a_c(t) = i\int_0^t dt' \exp\left[-i\int_0^{t'}\varepsilon_v(k(t''))dt''\right]E(t')\,X_{cv}(k(t'))$$

$$\times \exp\left[-i\int_{t'}^t \varepsilon_c(k(t''))dt''\right]. \quad \text{(C7)}$$

The time-dependent current is then

$$j(t) = a_v^*(t)a_c(t)X_{vc}[k(t)] + \text{c.c.}$$

$$= i\int_0^t X_{vc}(k(t))e^{-iS(t,t')}E(t')\,X_{cv}(k(t'))dt' + \text{c.c.}, \quad \text{(C8)}$$

where the action is

$$S(t,t') = \int_{t'}^t [\varepsilon_c(k(t'')) - \varepsilon_v(k(t''))]dt''. \quad \text{(C9)}$$

The three terms in (C8) correspond to recombination, propagation, and ionization, respectively, and the harmonic spectrum is calculated as the Fourier transform of the time-dependent current. By requiring the action to be stationary, we get two saddle-point conditions,

$$\varepsilon_c(k(t')) - \varepsilon_v(k(t')) = 0, \quad \text{(C10)}$$

$$\varepsilon_c(k(t)) - \varepsilon_v(k(t)) = E_r, \quad \text{(C11)}$$

where t' is the ionization time, t is the recombination time, and E_r is the recombination energy. We note that, compared to the gas-phase SFA, we have one less saddle-point equation (addressing the recollision time). This is because we have used the delocalized Bloch state as our initial condition, which is coupled to only one of the Houston states when the laser is on. In contrast, in the gas-phase SFA the ground state is localized in space and couples to multiple Volkov states.

The first saddle-point equation gives us the ionization time, while the second saddle-point equation gives the relation between the energy and the emission time of the emitted harmonic. For a simple vector potential $A = A_0 \sin(\omega t)$, the time-dependent crystal momentum is $k(t) = A_0 \sin \omega t$, and the solution to the first saddle-point equation is

$$t' = \frac{m\pi}{\omega} + i\gamma, \quad m = 0, \pm 1, \pm 2 \ldots. \quad \text{(C12)}$$

The real part of t' is the ionization time and the imaginary part γ is the VB-to-CB tunneling time at the band gap. The actual form of γ depends on the shape of the band structure around $k = 0$. To lowest order in k, the band structure around $k = 0$ can be approximated as

$$\varepsilon_c(k) - \varepsilon_v(k) \approx E_g + \frac{a}{2}k^2, \quad \text{(C13)}$$

where E_g is the band gap and a is an expansion coefficient. Then the saddle point equation [Eq. (C10)] becomes

$$E_g + \frac{a}{2}(A_0 \sin(\omega t'))^2 = 0, \quad \text{(C14)}$$

which gives

$$t' = \frac{m\pi}{\omega} + \frac{i}{\omega} \sinh^{-1}\left(\sqrt{\frac{2E_g}{aA_0^2}}\right). \quad (C15)$$

This means that the tunneling mostly happens at the time when the vector potential is 0, and the electron is at the minimum band gap for the two bands.

The second saddle-point equation then gives us the emission time for harmonics. For example, the energy of the emitted harmonic is maximized when the vector potential is at its maximum, and the recombination time for the cutoff harmonic

is therefore

$$t = \frac{(2n+1)\pi}{\omega}. \quad (C16)$$

The maximum energy of the harmonic is then

$$E_r = \varepsilon_c(A_0) - \varepsilon_v(A_0), \quad (C17)$$

which is just the maximum amount of the bands the vector potential can sample. We note that the treatment presented here is similar to that in [27], but here we stress a momentum-space three-step picture of the HHG process.

[1] M. Ferray, A. L'Huillier, X. F. Li, L. A. Lompre, G. Mainfray, and C. Manus, J. Phys. B **21**, L31 (1988).

[2] G. Farkas, C. Tóth, S. D. Moustaizis, N. A. Papadogiannis, and C. Fotakis, Phys. Rev. A **46**, R3605 (1992).

[3] S. Harris, J. Macklin, and T. Hänsch, Opt. Commun. **100**, 487 (1993).

[4] K. J. Schafer, B. Yang, L. F. DiMauro, and K. C. Kulander, Phys. Rev. Lett. **70**, 1599 (1993).

[5] P. B. Corkum, Phys. Rev. Lett. **71**, 1994 (1993).

[6] T. Brabec and F. Krausz, Rev. Mod. Phys. **72**, 545 (2000).

[7] G. Sansone, E. Benedetti, F. Calegari, C. Vozzi, L. Avaldi, R. Flammini, L. Poletto, P. Villoresi, C. Altucci, R. Velotta, S. Stagira, S. De Silvestri, and M. Nisoli, Science **314**, 443 (2006).

[8] F. Krausz and M. Ivanov, Rev. Mod. Phys. **81**, 163 (2009).

[9] J. Heber and A. Trabesinger, *Milestones: Photons* (Macmillan Publishers, 2010), pp. S5–S20.

[10] M. Hentschel, R. Kienberger, C. Spielmann, G. A. Reider, N. Milosevic, T. Brabec, P. Corkum, U. Heinzmann, M. Drescher, and F. Krausz, Nature **414**, 509 (2001).

[11] O. Smirnova, Y. Mairesse, S. Patchkovskii, N. Dudovich, D. Villeneuve, P. Corkum, and M. Y. Ivanov, Nature **460**, 972 (2009).

[12] H. J. Wörner, J. B. Bertrand, D. V. Kartashov, P. B. Corkum, and D. M. Villeneuve, Nature **466**, 604 (2010).

[13] T. Morishita, A.-T. Le, Z. Chen, and C. D. Lin, Phys. Rev. Lett. **100**, 013903 (2008).

[14] S. Ghimire, A. D. DiChiara, E. Sistrunk, P. Agostini, L. F. DiMauro, and D. A. Reis, Nat. Phys. **7**, 138 (2011).

[15] S. Ghimire, A. D. DiChiara, E. Sistrunk, U. B. Szafruga, P. Agostini, L. F. DiMauro, and D. A. Reis, Phys. Rev. Lett. **107**, 167407 (2011).

[16] O. Schubert, M. Hohenleutner, F. Langer, B. Urbanek, C. Lange, U. Huttner, D. Golde, T. Meier, M. Kira, S. W. Koch, and R. Huber, Nat. Photon. **8**, 119 (2014).

[17] M. Hohenleutner, F. Langer, O. Schubert, M. Knorr, U. Huttner, S. W. Koch, M. Kira, and R. Huber, Nature **523**, 572 (2015).

[18] F. Mahmood, C.-K. Chan, Z. Alpichshev, D. Gardner, Y. Lee, P. A. Lee, and N. Gedik, Nat. Phys. **12**, 306 (2016).

[19] G. Vampa, T. J. Hammond, N. Thiré, B. E. Schmidt, F. Légaré, C. R. McDonald, T. Brabec, and P. B. Corkum, Nature **522**, 462 (2015).

[20] G. Ndabashimiye, S. Ghimire, M. Wu, D. A. Browne, K. J. Schafer, M. B. Gaarde, and D. A. Reis, Nature **534**, 520 (2016).

[21] M. Korbman, S. Yu. Kruchinin, and V. S. Yakovlev, New J. Phys. **15**, 013006 (2013).

[22] A. F. Kemper, B. Moritz, J. K. Freericks, and T. P. Devereaux, New J. Phys. **15**, 023003 (2013).

[23] G. Vampa, C. R. McDonald, G. Orlando, D. D. Klug, P. B. Corkum, and T. Brabec, Phys. Rev. Lett. **113**, 073901 (2014).

[24] T. Higuchi, M. I. Stockman, and P. Hommelhoff, Phys. Rev. Lett. **113**, 213901 (2014).

[25] P. G. Hawkins, M. Y. Ivanov, and V. S. Yakovlev, Phys. Rev. A **91**, 013405 (2015).

[26] M. Wu, S. Ghimire, D. A. Reis, K. J. Schafer, and M. B. Gaarde, Phys. Rev. A **91**, 043839 (2015).

[27] G. Vampa, C. McDonald, A. Fraser, and T. Brabec, IEEE J. Select. Top. Quantum Electron. **21**, 8700110 (2015).

[28] G. Vampa, C. R. McDonald, G. Orlando, P. B. Corkum, and T. Brabec, Phys. Rev. B **91**, 064302 (2015).

[29] C. R. McDonald, G. Vampa, P. B. Corkum, and T. Brabec, Phys. Rev. A **92**, 033845 (2015).

[30] Z. Guan, X.-X. Zhou, and X.-B. Bian, Phys. Rev. A **93**, 033852 (2016).

[31] G. Vampa, T. J. Hammond, N. Thiré, B. E. Schmidt, F. Légaré, C. R. McDonald, T. Brabec, D. D. Klug, and P. B. Corkum, Phys. Rev. Lett. **115**, 193603 (2015).

[32] J. B. Krieger and G. J. Iafrate, Phys. Rev. B **33**, 5494 (1986).

[33] V. P. Krainov and V. P. Yakovlev, Zh. Eksp. Teor. Fiz. **78**, 2204 (1980) [Sov. Phys. JETP **51**, 1104 (1980)].

[34] I. Sh. Averbukh and N. F. Perelman, Zh. Eksp. Teor. Fiz. **88**, 1131 (1985) [Sov. Phys. JETP **61**, 665 (1985)].

[35] L. Plaja and L. Roso-Franco, J. Opt. Soc. Am. B **9**, 2210 (1992).

[36] M. Y. Ivanov, P. B. Corkum, and P. Dietrich, Laser Phys. **3**, 375 (1993).

[37] V. Krainov and Z. Mulyukov, Laser Phys. **4**, 544 (1994).

[38] F. I. Gauthey, B. M. Garraway, and P. L. Knight, Phys. Rev. A **56**, 3093 (1997).

[39] A. Santana, J. M. G. Llorente, and V. Delgado, J. Phys. B **34**, 2371 (2001).

[40] C. Figueira de Morisson Faria and I. Rotter, Phys. Rev. A **66**, 013402 (2002).

[41] P. Haljan, T. Fortier, P. Hawrylak, P. B. Corkum, and M. Y. Ivanov, Laser Phys. **13**, 452 (2003).

[42] C. F. de Morisson Faria and I. Rotter, Laser Phys. **13**, 985 (2003).

[43] S. Ashhab, J. R. Johansson, A. M. Zagoskin, and F. Nori, Phys. Rev. A **75**, 063414 (2007).

[44] A. Picón, L. Roso, J. Mompart, O. Varela, V. Ahufinger, R. Corbalán, and L. Plaja, Phys. Rev. A **81**, 033420 (2010).

[45] H. K. Avchyan, B. R. Avchyan, and G. F Mkrtchian, J. Phys. B **45**, 25402 (2012).

[46] B. M. Garraway and S. Stenholm, Phys. Rev. A **45**, 364 (1992).

[47] Wolfram Research Inc., *Mathematica 11.0* (Wolfram Research, Champaign, IL, 2016); see Continuous Wavelet Transform.

[48] J. C. Slater, Phys. Rev. **87**, 807 (1952).

[49] R. D. Jaffe, Am. J. Phys. **78**, 620 (2010).

[50] M. Lewenstein, P. Balcou, M. Y. Ivanov, A. L'Huillier, and P. B. Corkum, Phys. Rev. A **49**, 2117 (1994).

[51] M. Lewenstein, P. Salières, and A. L'Huillier, Phys. Rev. A **52**, 4747 (1995).

[52] D. B. Milošević, G. G. Paulus, D. Bauer, and W. Becker, J. Phys. B **39**, R203 (2006).